electrochem

MDPI

Article

Electrochemical Sensing of Hydrogen Peroxide Using Composite Bismuth Oxide/Bismuth Oxyselenide Nanostructures: Antagonistic Influence of Tungsten Doping

Pooja D. Walimbe †, Rajeev Kumar *,†, Amit Kumar Shringi, Obed Keelson, Hazel Achieng Ouma and Fei Yan *

Department of Chemistry and Biochemistry, North Carolina Central University, Durham, NC 27707, USA; pwalimbe@eagles.nccu.edu (P.D.W.); ashringi@nccu.edu (A.K.S.); okeelson@eagles.nccu.edu (O.K.); houma@eagles.nccu.edu (H.A.O.)

* Correspondence: rkumar@nccu.edu (R.K.); fyan@nccu.edu (F.Y.)

† These authors contributed equally to this work.

Abstract: This study investigates the underlying mechanisms of hydrogen peroxide (H_2O_2) sensing using a composite material of bismuth oxide and bismuth oxyselenide ($Bi_2O_xSe_y$). The antagonistic effect of tungsten (W)-doping on the electrochemical behavior was also examined. Undoped, 2 mol%, 4 mol%, and 6 mol% W-doped $Bi_2O_xSe_y$ nanostructures were synthesized using a one-pot solution phase method involving selenium powder and hydrazine hydrate. W-doping induced a morphological transformation from nanosheets to spherical nanoparticles and amorphization of the bismuth oxyselenide phase. Electrochemical sensing measurements were conducted using cyclic voltammetry (CV) and differential pulse voltammetry (DPV). H_2O_2 detection was achieved over a wide concentration range of 0.02 to 410 μM. In-depth CV analysis revealed the complex interplay of oxidation-reduction processes within the bismuth oxide and Bi_2O_2Se components of the composite material. W-doping exhibited an antagonistic effect, significantly reducing sensitivity. Among the studied samples, undoped $Bi_2O_xSe_\gamma$ demonstrated a high sensitivity of 83 μA μM^{-1} cm^{-2} for the CV oxidation peak at 0 V, while 6 mol% W-$Bi_2O_xSe_y$ became completely insensitive to H_2O_2. Interestingly, DPV analysis showed a reversal of sensitivity trends with 2 and 4 mol% W-doping. The applicability of these samples for real-world analysis, including rainwater and urine, was also demonstrated.

Keywords: bismuth oxyselenide; nanosheets; hydrogen peroxide; sensing; electrochemistry

Citation: Walimbe, P.D.; Kumar, R.; Shringi, A.K.; Keelson, O.; Ouma, H.A.; Yan, F. Electrochemical Sensing of Hydrogen Peroxide Using Composite Bismuth Oxide/Bismuth Oxyselenide Nanostructures: Antagonistic Influence of Tungsten Doping. *Electrochem* **2024**, *5*, 455–469. https://doi.org/10.3390/electrochem5040030

Academic Editor: Masato Sone

Received: 30 August 2024
Revised: 13 October 2024
Accepted: 21 October 2024
Published: 24 October 2024

1. Introduction

Hydrogen peroxide (H_2O_2) is an important chemical employed in various industries and also plays a vital role in environmental and physiological processes. H_2O_2 is a common disinfectant [1] and a strong oxidizing agent [2]. It is used in oxidation reactions for breaking down organic compounds. Due to its disinfecting properties, it is widely used in pharmaceutical industries for sanitizing surfaces, medical equipment, and in wound care. In industries such as textile manufacturing, pulp, and paper production, H_2O_2 serves as a bleaching agent. H_2O_2 is being used as an antioxidant in food industries; in this case, acting as an effective reductant. H_2O_2 is classified as a reactive oxygen species (ROS) at the cellular level, playing a crucial role in several biological processes such as cell proliferation, immune response, root development, and programmed cell death (apoptosis) [3–7].

While H_2O_2 has numerous beneficial uses, it can also cause harmful effects, especially when used in high concentrations. For instance, inhaling H_2O_2 vapors beyond safe exposure levels can irritate the respiratory system, resulting in symptoms like coughing, difficulty breathing, chest discomfort, and throat irritation [8]. Direct exposure to concentrated H_2O_2 can cause skin and eye irritation and chemical burns. An increased level of H_2O_2 due to increased production can adversely affect the human body by damaging the

normal cells and causing cancer [9]. In recent years, various traditional methods have been employed for H_2O_2 detection, including enzymatic assays [2,10,11], titrimetry [12], fluorescence [13], colorimetry [14], chromatography [15], and electrochemistry [10,16–20].Among these, electrochemical sensing has gained much attention as it offers several advantages, including high sensitivity, rapid response, and the ability to perform real-time measurements [20]. Hence, accurate, and sensitive detection of H_2O_2 is vital for understanding its biological roles, ensuring product safety, protecting the environment, and optimizing industrial processes.

Recently, Bi_2O_2Se, a bismuth-based oxychalcogenide, has been gaining much attention in electronic and optoelectronic applications [21–29]. In this material, positively charged $[Bi_2O_2]^{2+}$ and negatively charged Se^{2-} layers are alternatively stacked together to form a tetragonal structure [30]. This material not only offers high carrier mobility (>20,000 cm^2 V^{-1} s^{-1} at 2 K) [24,26,31–33], but it also has a bandgap of 0.8 eV and remarkable thermal and chemical stability. Some of the studies have already discussed its selectivity towards H_2O_2 detection [16,34]. As doping alters the electronic properties of a semiconductor, we hypothesize that doping this material with tungsten, which is one of the catalytically important transition metals, will alter and improve the sensing capability. Herein, we synthesized 2, 4, and 6 mol% W-doped bismuth oxyselenide nanosheets at room temperature using a modified synthesis method developed by Chitara et al. [16] for electrochemical sensing of H_2O_2. Recently, in our group, we discovered that a composite Bi_2O_3/Bi_2O_2Se (or $Bi_2O_xSe_y$) shows better H_2O_2 sensing than pristine Bi_2O_2Se [34]. Therefore, in this work, we use a similar sample and study the influence of W-doping on the detection capabilities. This study provides valuable mechanistic insights into the electrochemical detection of H_2O_2 using bismuth oxide and bismuth oxyselenide ($Bi_2O_xSe_y$) composites, particularly examining the impact of W-doping. We observed significant transformations in morphology and phase, with W-doping leading to the formation of spherical nanoparticles and amorphization of the bismuth oxyselenide phase. Electrochemical analysis using CV and DPV revealed a complex interplay of redox reactions.

2. Material and Methods

2.1. Materials and Reagents

For the experiments, the following materials were used: Bismuth nitrate pentahydrate ($Bi(NO_3)_3{\cdot}5H_2O$) (Thermo Scientific, Fair Lawn, NJ, USA), sodium tungstate dihydrate (Thermo Scientific, Fair Lawn, NJ, USA), Se powder (Alfa Aesar), KOH (Fischer Scientific, Pittsburgh, PA, USA), NaOH (Fischer Scientific, Pittsburgh, PA, USA), ethylenediaminetetraacetic acid (EDTA, Across Organics, Waltham, MA, USA), hydrazine hydrate ($N_2H_4{\cdot}H_2O$, 64%) (Thermo Scientific, Fair Lawn, NJ, USA), Nafion solution (5% in small alcohols, Sigma Aldrich, St. Louis, MO, USA), isopropyl alcohol (Merck, St. Louis, MO, USA), and deionized water (DI water, <18 Ω). Hydrogen peroxide (30%, Fischer Scientific, Pittsburgh, PA, USA) was employed as the analyte, while phosphate-buffered saline (PBS, pH 7.4, 1X molarity) served as the electrolyte.

2.2. Synthesis of W-Doped $Bi_2O_xSe_y$

$Bi_2O_xSe_y$ nanosheets with tungsten doping levels of 2, 4, and 6 mol% were prepared using a solution-phase method, with the mol% calculated relative to bismuth. The procedure for synthesizing the undoped sample, previously detailed in earlier research [34], involved dissolving 1 g of $Bi(NO_3)_3{\cdot}5H_2O$ in 200 mL of deionized water, followed by 30 min of sonication. A solution of Se powder (80 mg) in 10 mL of $N_2H_4{\cdot}H_2O$ was then added to the mixture under constant stirring, along with 3 g of EDTA. Subsequently, 1.2 g of KOH and 3.2 g of NaOH were added, leading to the formation of $Bi_2O_xSe_y$ nanosheets, as indicated by the black coloration. The mixture was stirred for 18 h, allowed to rest, and the resulting dark brown precipitate was centrifuged at 5000 rpm, washed with water and ethanol, and dried at 80 °C. For the W-doped samples, stoichiometric amounts of $Bi(NO_3)_3{\cdot}5H_2O$ and sodium tungstate were used, keeping all the other parameters same.

2.3. Material Characterization

Powder X-ray Diffraction (XRD) data were obtained using an XRDynamic 500 diffractometer (Anton Paar), which was equipped with a Cu source and operated at 45 keV and 40 kW. The morphology and elemental composition were analyzed using a FEI XL30 SEM-FEG Scanning Electron Microscope, along with an Energy Dispersive X-ray (EDX) analysis for elemental mapping. The X-ray Photoelectron Spectroscopy (XPS) analyses in the study utilized a Physical Electronics VersaProbe III instrument with a monochromatic Al K_α X-ray source for surface characterization. The charge neutralization was achieved through low-energy electrons and argon ions, with binding energy calibration referencing copper and gold standards. This setup allowed for the identification of bismuth compounds, focusing on Bi^{3+}. For homogeneous samples, major elements (>5 atom%) typically showed standard deviations of less than 3%, while minor elements had significantly higher deviations. The analysis area was approximately 200 µm in diameter. UV-Visible-Near Infrared Spectra (UV-Vis-NIR) were recorded on a Shimadzu UV-Visible-NIR spectrometer equipped with a Harrick Praying Mantis Diffuse Reflection Accessory. Spectra were referenced to a KBr background. All electrochemical characterizations were carried out on a Waverider-200 Bipotentiostat (Pine Research).

2.4. Fabrication of Working Electrode

The glassy carbon electrode (GCE) with a circular area of 0.07 cm^2 was used for electrochemical analysis. Before fabrication, the electrode was polished using different particle sizes of alumina powder. It was then washed with DI and ethanol and dried in an oven. For the electrochemical tests, nanocomposite dispersions were prepared by mixing 5 mg of the samples in a 9:1 ratio of isopropanol (IPA)/DI water (i.e., 900 µL of IPA and 100 µL of DI water), with the addition of 100 µL of Nafion solution. A 2.5 µL portion of this dispersion was drop-cast onto the polished GCE.

2.5. Electrochemical Sensing Characteristics

For electrochemical measurements, a three-electrode system was used to detect H_2O_2. The setup consisted of a GCE, a coiled Pt wire, and anAg/AgCl reference electrode. All electrodes were purchased from BAS Inc. CV and DPV were conducted in PBS, with stirring and argon gas purging for enhanced detection precision.

The electrochemical measurements were conducted in a voltammetric cell containing 15 mL of PBS, which was purged with argon for 30 min and stirred at 400 rpm. Stirring and purging were paused during CV and DPV scans. The potential window ranged from 0.8 V to −0.9 V versus Ag/AgCl at a scan rate of 10 mV/s, starting at 0 V. The initial scan direction was positive. In DPV, the pulse parameters were 50 mV in height, 0.01 s in width, 0.1 s step period, and 10 mV potential increment, scanning from 0.8 V to −0.9 V without inversion during sweeps.

To evaluate the sensing, 150 µL of a 2 µM H_2O_2 stock solution was initially introduced, diluting the concentration by a factor of 100. Purging and stirring were repeated for 5 min after each H_2O_2 addition. Stock solutions of 2, 20, 200, 1000, and 10,000 µM were prepared, with sensitivity (S) calculations based on the effective concentrations at each stage.

3. Results and Discussion

3.1. Structural, Morphological and Optical Characterization

The powder XRD patterns are presented in Figure 1, along with standard data from the Inorganic Crystal Structure Database (ICSD) for comparison. The pristine sample prepared without W-doping showed a composite structure that resembles α-Bi_2O_3 (ICSD code: 2374) and Bi_2O_2Se (ICSD code: 2903). Upon W-doping, the peaks from Bi_2O_2Se seem to disappear and a broad amorphous peak appears ($2\theta \approx 22$–32°). Ghosh et al. [33] and Chitara et al. [16] have also observed similar broad peaks for amorphous-type as-synthesized Bi_2O_2Se with short synthesis times. The intensity of the amorphous peak increases with W-doping (Figure 1b). It can be rationalized that tungsten preferably coordinates with Se^{2-} and forms

the amorphous W-doped bismuth oxyselenide component. The XRD patterns for all doped samples show a dominant Bi_2O_3 phase with the absence of any crystalline Bi_2O_2Se.

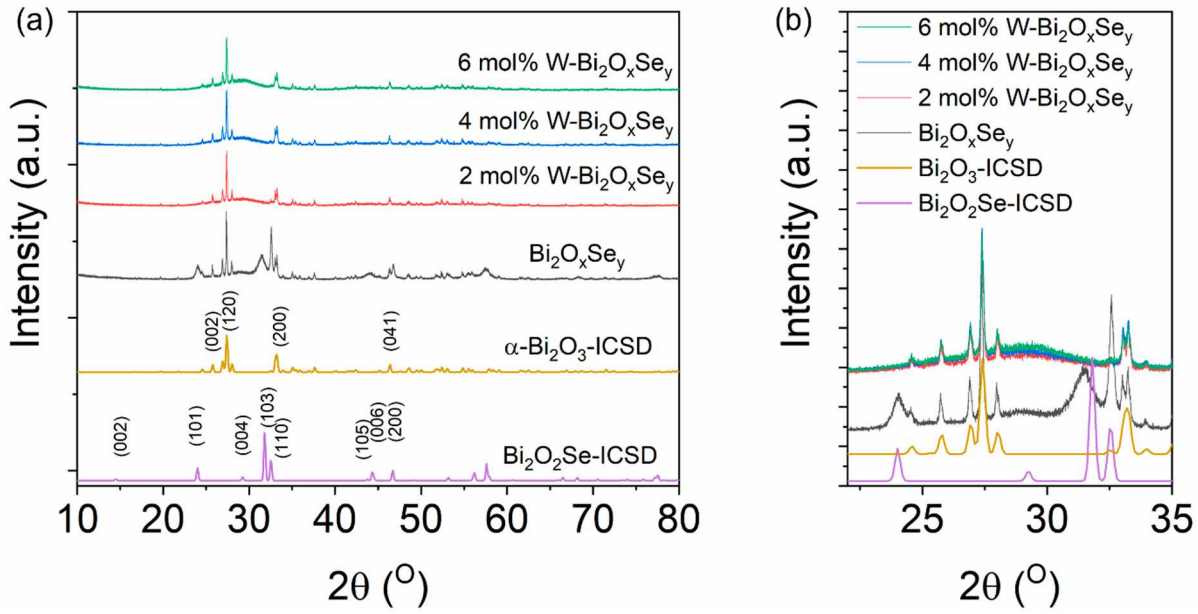

Figure 1. (**a**) XRD patterns of undoped, 2, 4, and 6 mol% W-doped $Bi_2O_xSe_y$ samples. (**b**) A zoomed-in view of the XRD patterns highlights the amorphous phase and structural transformation.

The SEM analyses (Figure 2a–d) reveal nanosheet formation in all samples. The EDX spectrum of the representative 4 mol% W-doped $Bi_2O_xSe_y$ sample confirms the presence of Bi, W, O, and Se. For the SEM-EDX measurements, the powder sample was sprinkled onto an Ir-coated silicon wafer, which was stuck onto an aluminum stub using carbon tape. The additional peaks of C and Ir observed in the EDX originate from these and not from the material.

The XPS analyses (Figures 3 and S1, Supporting Information, ESI) confirms the presence of Bi, Se, W, and O in the sample. Although accurate quantification for W could not be estimated with confidence, the presence of both W and Se is qualitatively confirmed. Furthermore, in the Se 3d spectrum, 3 sub-peaks can be observed. The peaks around 54 and 55.5 eV belong to 3d 5/2 and 3d 3/2, respectively, corresponding to the metal selenide phase. This suggests that Se is coordinated with Bi as well as with W, within the Bi_2O_2Se component. The peak at 59 eV is from the Se–O bond. The UV-Vis-NIR DRS and corresponding Tauc plots are presented in Figure S2 (ESI). The band gap increase as a function of doping indicates the formation of relatively more oxide phase. As can be observed in the case of the undoped sample, there are two linear regimes in Figure S2b, which can result from the two-component phases (Bi_2O_2Se and Bi_2O_3). With 6 mol% W-doping, the absorption coefficient (y-axis) is quite low, and this indicates more amorphization of the sample. Furthermore, the area under the curve below 2.3 eV in the Tauc plots is highest for 4 mol% W-doped $Bi_2O_xSe_y$. This region signifies the 'density of defects' and can serve as an indication for optimal electronic transition.

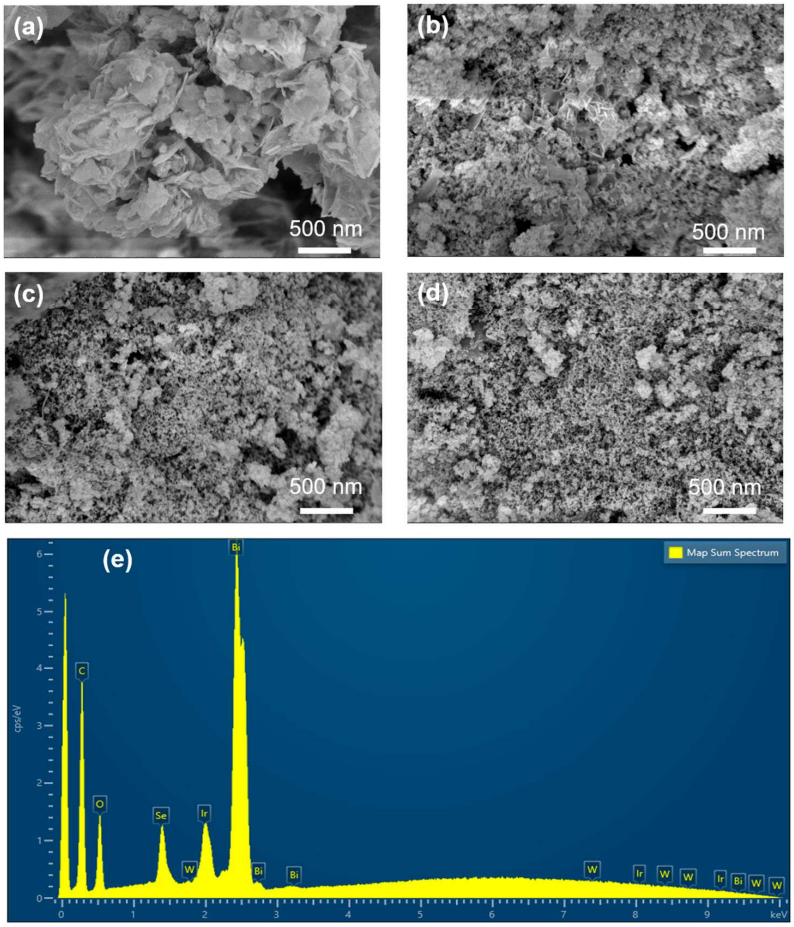

Figure 2. SEM images for (**a**) undoped, (**b**) 2, (**c**) 4, and (**d**) 6 mol% W-doped $Bi_2O_xSe_y$ samples. (**e**) EDX spectrum for 4 mol% W-doped $Bi_2O_xSe_y$ sample.

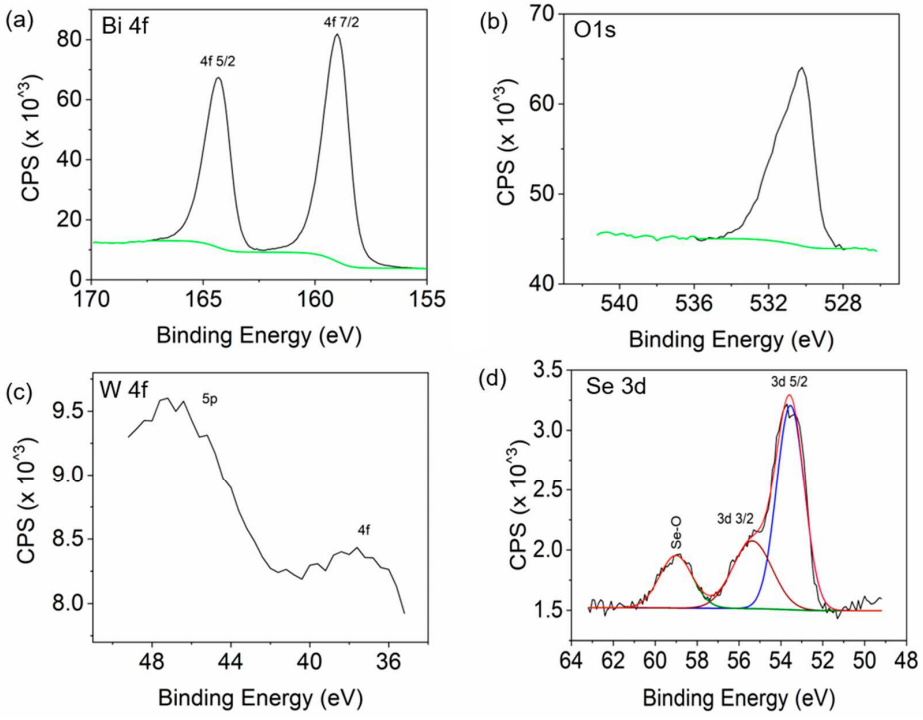

Figure 3. High resolution XPS for (**a**) Bi, (**b**) O, (**c**) W, and (**d**) Se, for 4 mol% W-$Bi_2O_xSe_y$ sample. In (**d**) the red line is the cumulative fit, while other colour lines are the fits for the sub-peaks.

3.2. Electrochemical Sensing Performance

Electrochemical sensitivity to H_2O_2 was evaluated using CV and DPV. For both techniques, a potential range between 0.8 to −0.9 V was set against the Ag/AgCl electrode. Sensitivity towards H_2O_2 was obtained by plotting the CV and DPV peak current versus effective concentration of the analyte, and evaluated as per the equation: S = k/A, [17], where k is the slope of the calibration plot and A is the area of the GCE in cm^2. Scheme 1 depicts the protocol used in the modification of the GCE.

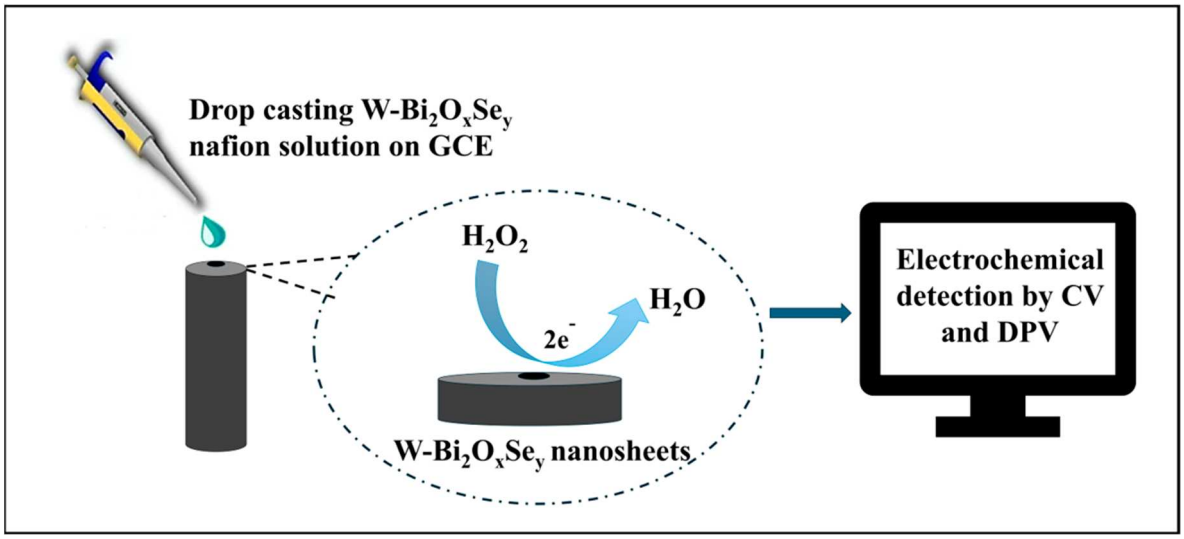

Scheme 1. Protocol for estimating the electrochemical sensing on GCE using a three-electrode setup.

3.3. CV Analyses

Figure 4a depicts the selective CV scans in the blank electrolyte (50 cycles) with a scan rate of 10 mV/s. In the first cycle, there is no reduction peak and only one oxidation peak (around +0.15 V) is observed. In subsequent cycles, new peaks emerge and this oxidation peak also shifts towards the right. At the end of the 50th cycle, we observe three prominent oxidation peaks and two prominent reduction peaks (Table S1, ESI). The reduction peak at −0.57 V is observable only for the first few cycles and a clear transformation and intensification of the reduction peaks at −0.64 and −0.7 V is observed. However, the oxidation peak around 0 V intensifies and does not shift. Figure 4b shows the CV scans at different scan rates (after 50 cycles at 10 mV/s). The electrode diffusion kinetics are estimated for the prominent oxidation (0 V) and reduction (most intense) peaks, by plotting the current vs. square root of the scan rate. It is clear from the slopes in Figure 4c that the reduction kinetics occur faster than oxidation. It becomes clear that the material undergoes phase transformation during consecutive electrochemical cycling even in the blank electrolyte.

Figure 4d depicts the CV scans (10 mV/s) with increasing concentrations of H_2O_2, which was sequentially added to the electrolyte. The H_2O_2 concentrations were varied in the range of 0.02 to 410 µM (stock concentration: 2–10,000 µM). The oxidation peak at 0 V and the reduction peak at −0.7 V show an increasing trend, whereas the oxidation peak (~0.28 V) first increases and then decreases in intensity with high H_2O_2 amounts. For evaluation of the sensitivity, both oxidation and reduction peaks are considered (Figure 4e,f) and the results are presented in Table 1. The linear range over which the electrode is sensitive is 0–15 µM. The CV scans for H_2O_2 addition without prior stabilization show significant peak shifting, making the analysis tricky and less consistent (Figure S3, ESI).

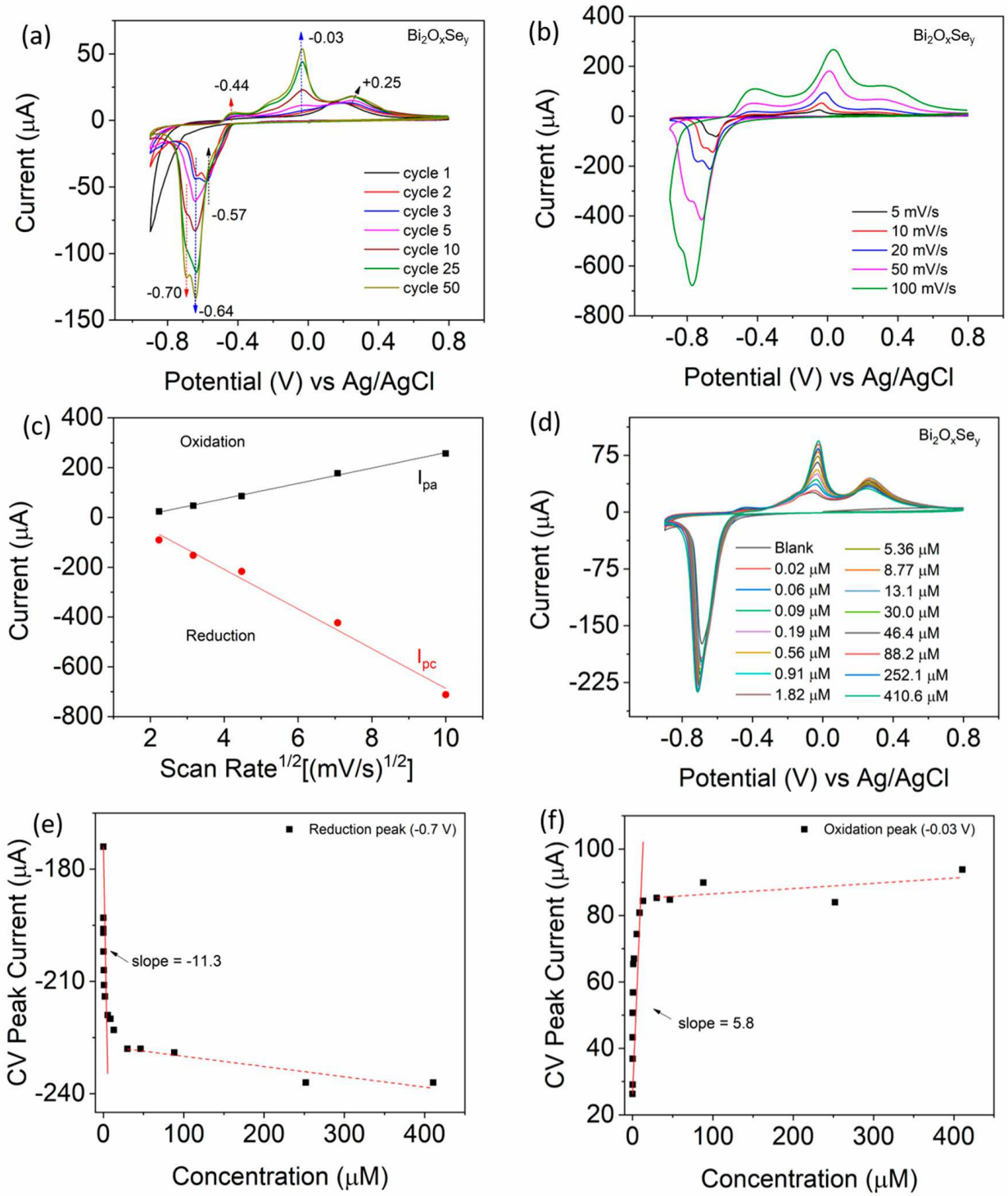

Figure 4. CV analyses for $Bi_2O_xSe_y$: (**a**) CV in blank electrolyte run for 50 cycles at 10 mV/s. (**b**) CV in blank electrolyte at different scan rates after stabilization. (**c**) Plot of CV peak current vs. square root of scan rate. (**d**) CV with increasing concentration of H_2O_2, incrementally added post stabilization. (**e**) Plot of reduction peak current vs. concentration. (**f**) Plot of oxidation peak current vs. concentration. The black squares represent the peak current, the solid red lines represent the linear fits, and the dotted red lines indicate the non-sensitive regime.

Table 1. Sensitivity values were calculated from CV and DPV data. The negative slope of the linear fit indicates an inverse relationship between current and H_2O_2 concentration.

Sample	Sensitivity (CV) ($\mu A\ \mu M^{-1}\ cm^{-2}$)		Sensitivity (DPV) ($\mu A\ \mu M^{-1}\ cm^{-2}$)
	Reduction Peak (−0.7 V)	Oxidation Peak (~0 V)	(−0.73 V)
$Bi_2O_xSe_y$	−161	83	57
2 mol% W-$Bi_2O_xSe_y$	−56	16	−1.4
4 mol% W-$Bi_2O_xSe_y$	−27	3.1	−28

The CV scans for the doped samples (after stabilization for 50 cycles) with increasing H_2O_2 concentrations are plotted in Figure 5. Although multiple redox peaks are observed in undoped $Bi_2O_xSe_y$ sample, possibly originating from different chemical environments of Bi-O and Bi-Se, the oxidation peak around +0.3 V and the reduction peak around −0.57 V are completely absent in the doped samples. Most probably, this set of redox peaks probably belongs to the semi-crystalline Bi_2O_2Se component. The sensitives for both oxidation and reduction peaks are evaluated in the same manner as aforementioned. It is clear from the slope values that the sensitivity towards H_2O_2 falls upon W-doping. This can be due to the transformation of composite nanosheets to Bi_2O_3 dominant spherical particles. In our earlier work, we had a similar observation where Bi_2O_3 nanomaterial showed poor sensitivity than undoped composite $Bi_2O_xSe_y$ [34]. It can also be seen from Figure 5g–i that the 6 mol% W-$Bi_2O_xSe_y$ is completely insensitive to H_2O_2. Therefore, no attempt is made to fit the data points.

We hypothesize that the observed redox peaks are associated with the metal oxide and metal selenide components. Across all samples, the first cycle of cyclic voltammetry (CV) shows no reduction peak, while oxidation peaks are present from the initial cycle. In subsequent cycles, a distinct reduction peak appears, which becomes more pronounced with the addition of H_2O_2. This indicates that chemical reactions are likely occurring between the electrolyte and the electrode material. The redox peaks most likely originate from the metal oxide/selenide composite rather than solely from the electroreduction of H_2O_2. In the presence of H_2O_2, preferential oxidation of the selenide may enhance the peak intensity for the oxide component.

Based on these observations, a reaction mechanism is proposed, as below.

$$Bi_2O_xSe_y + aH_2O \leftrightarrow Bi_2O_{(x+a)}Se_y + a\left(2H^+\right)\ \text{(Partially oxidized)} \quad (1)$$

$$Bi_2O_{(x+a)}Se_y + bH_2O_2 \leftrightarrow Bi_2O_{(x+a+2b)}Se_y + b\left(2H^+\right)\ \text{(More oxidized)} \quad (2)$$

To evaluate the reusability of the electrode, we conducted three separate CV experiments using the same electrode (undoped) with fresh electrolytes for each trial (Figure S4, ESI). Before each experiment, the electrode was gently rinsed with DI water and allowed to dry at 80 °C. The results consistently exhibited similar behavior across all trials. In every measurement, an increasing trend in current response was observed as the H_2O_2 concentration increased.

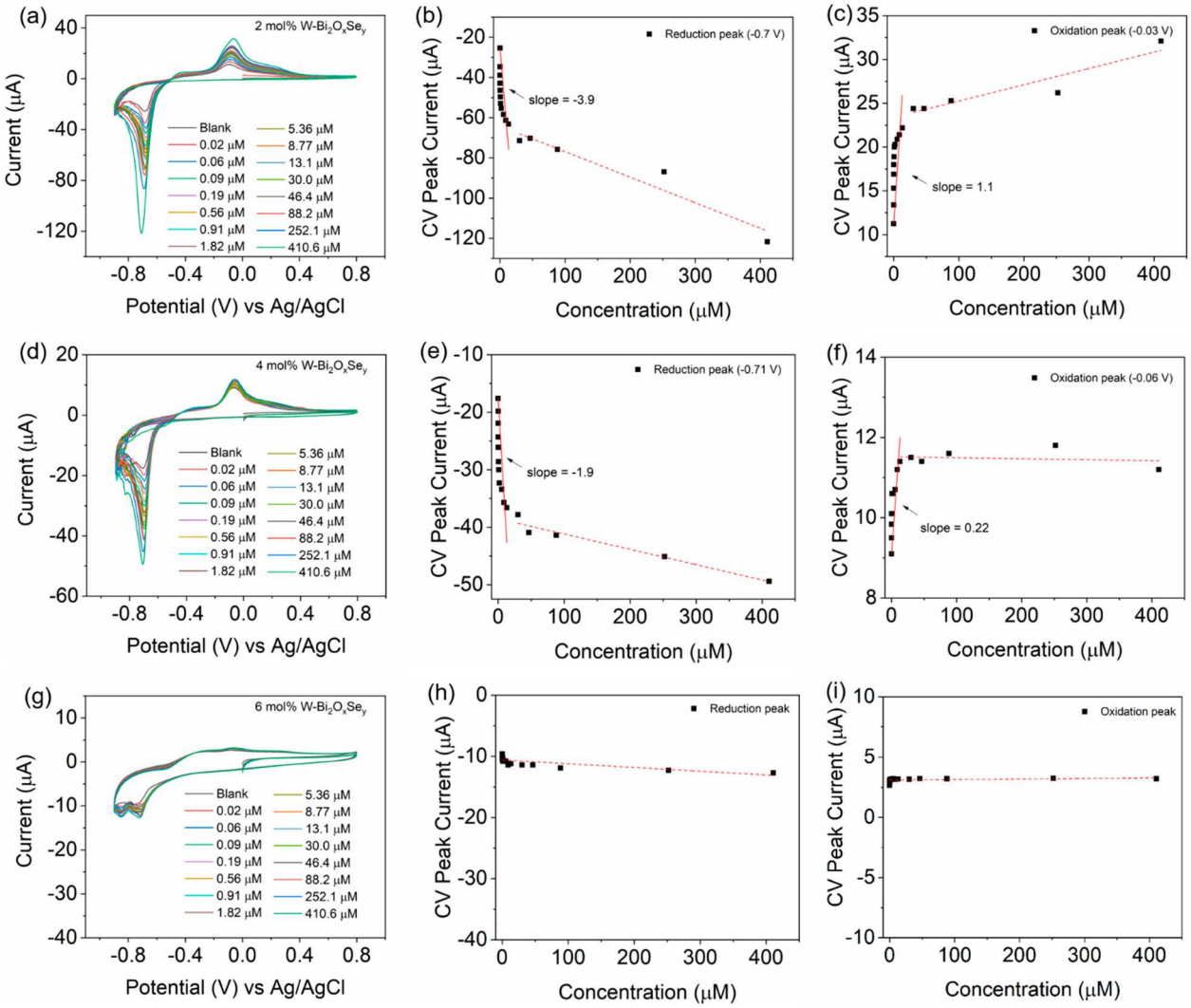

Figure 5. Left panel: CV scans for (**a**) 2, (**d**) 4, and (**g**) 6 mol% tungsten-doped $Bi_2O_xSe_y$ samples. Middle panel: Linear fits of the CV reduction peak current (at approximately −0.7 V) with respect to H_2O_2 concentration of (**b**) 2, (**e**) 4, and (**h**) 6 mol% W-doped $Bi_2O_xSe_y$ samples to determine the sensitivity. Right panel: linear fits of the CV oxidation peak current (at approximately 0 V) with respect to H_2O_2 concentration of (**c**) 2, (**f**) 4, and (**i**) 6 mol% W-doped $Bi_2O_xSe_y$ samples to determine the sensitivity. The black squares represent the peak current, the solid red lines represent the linear fits, and the dotted red lines indicate the non-sensitive regime.

3.4. DPV Analyses

The DPV scans (Figure 6) show a single peak per scan for all samples. The trend in the DPV peak current value appears slightly different from that observed for the reduction peak in CV. Since 6 mol% W-$Bi_2O_xSe_y$ is completely insensitive to H_2O_2, as seen in CV, we do not evaluate it further. For obtaining a good coefficient of determination (R^2), we have used the entire range of studied H_2O_2 concentrations yielding a greater number of data points. As can be seen in Figure 6, the data can be clubbed into two distinct regions. Region 1 (0–15 μM) shows much higher sensitivity although in a much smaller concentration range. This plot represents the average results from three independent experiments, each conducted with new electrode-electrolyte setups. The sensitivity is evaluated considering the slope values of the linear fit in the first region which shows a high slope. The values are given in Table 1.

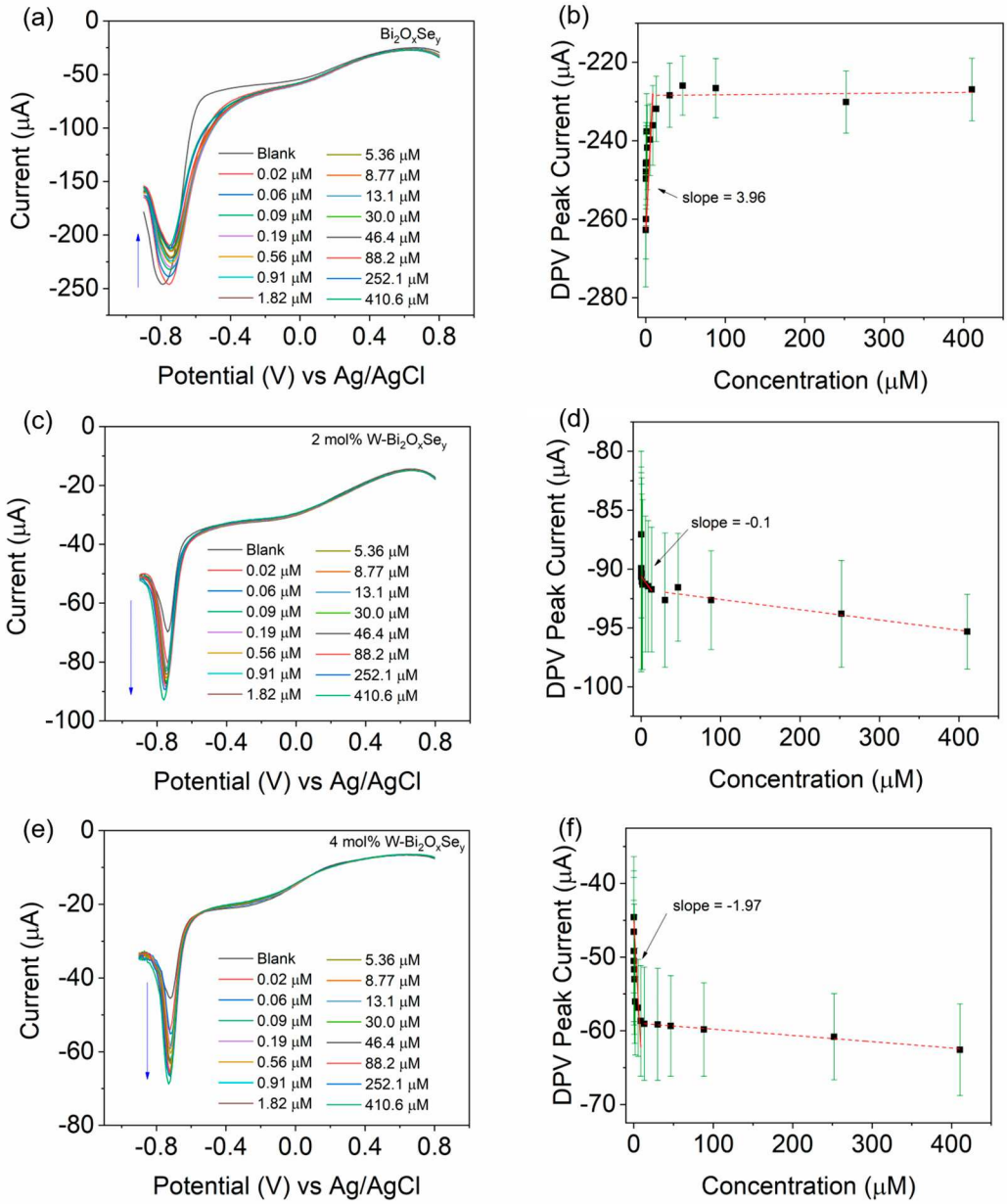

Figure 6. Left panel: DPV scans of (**a**) undoped, (**c**) 2, and (**e**) 4 mol% W-doped $Bi_2O_xSe_y$ samples. Right panel: Linear fits of the DPV peak current (at approximately −0.7 V) with respect to H_2O_2 concentration of (**b**) undoped, (**d**) 2, and (**f**) 4 mol% W-doped $Bi_2O_xSe_y$ samples to determine the sensitivity. The black squares represent the average data of three fresh experiments, the solid red lines represent the linear fits, and the standard errors are presented as green color lines. The dotted red lines indicate the non-sensitive regime.

An interesting observation is the change in slope characteristics in region 1, with the increase in W-doping. With 2 mol% W-doping the slope reverses and decreases drastically with respect to the undoped sample. The slope value further lowers with 4 mol% W-doping. This suggests that the reaction kinetics (and probably the mechanism) change upon W-doping; 4 mol% W-doping probably stabilizes the composite structure to a greater degree compared to 2 mol% W-doping.

Considering the CV and DPV results together, we observe that the sensitivity values are quite different in both techniques. The DPV technique is relatively faster and simpler to analyze. However, in these materials, the CV reduction peak and DPV peak can show a significant shift. It is only the oxidation peak at ~0 V that appears invariant. We propose that

the CV analyses of this oxidation peak can be a better tool to evaluate the H_2O_2 sensitivity in such complex situations. Table 2 presents a comparison of the sensing performance with selected published literature.

Table 2. Comparative electrochemical sensing performance with published literature.

Sensing Material	CV/DPV Peak	Sensitivity	Detection Range	Limit of Detection (LoD)	pH	Reference
Bi_2O_3/MnO_2	0.8 V	0.914 μA $μM^{-1}$ cm^{-2}	0.2–290 μM	0.05 μM	7.2	[35]
NF/HRP/Bi_2O_3–WCNT/GCE	−0.3 V	26.54 μA mM^{-1} cm^{-2}	8.34–28.88 mM	-	7	[36]
Bi_2Se_3–Hb–Nf/GCE	−0.3 V	-	2.0–100 μM	0.63 μM	7	[18]
Bi_2S_3/g-C_3N_4	0.26 V	1011 μA $μM^{-1}$ cm^2	0.5–950 μM	0.078 μM	12	[19]
BOSe-6 h	−0.7 V	75.7 μA $μM^{-1}$ cm^{-2}	0–15 μM	-	7.4	[34]
Bi_2O_2Se nanosheets	−0.68 V	100 μA $μM^{-1}$ cm^{-2}	50–500 μM		7.4	[16]
$Bi_2O_xSe_y$	0 V	83 μA $μM^{-1}$ cm^{-2}	0–15 μM	-	7.4	This Work

3.5. Real Sample Analyses

Furthermore, for practical applications of these materials as H_2O_2 sensors, we tested the fabricated electrodes (undoped and 4 mol% W-doped $Bi_2O_xSe_y$) using rainwater collected during a thunderstorm (hurricane Helene passing over Durham, North Carolina, dated 27 September 2024) and real urine (from a diabetic individual). The DPV technique was used as it is faster (a few seconds) compared to CV (a few minutes). In both cases, we first added 150 μL of the real sample in 15 mL of 1X PBS, followed by 300 μL of sequential addition. Argon gas purging and stirring were maintained during each addition. For the assessment of the rainwater sample, 30 readings were recorded, while we measured 10 readings in the case of urine samples. We only present a few DPV scans for data clarity. The slopes of the calibration curves (Figure 6b,f) were used to estimate the range of H_2O_2 in both the real samples. In case of both rainwater and urine, the DPV scans (Figure 7a,b,e,f) show an 'inhibitive' character for both electrodes. The box charts are presented in Figure 7c,d,g,h.

The estimated range for H_2O_2 in rainwater is 5–15 μM. The median value is ~11 μM. The value obtained with the undoped sample can be considered more accurate as the measurement was carried out immediately after collection. The measurement with 4 mol% W-doped $Bi_2O_xSe_y$ was conducted after a few days, which could have led to some loss of H_2O_2 during storage.

In the case of urine samples, both electrodes yield a similar range for measurements carried out within a timeframe of a few hrs. The estimated range for H_2O_2 in the urine was similar for both electrodes, i.e., 3–11 μM. The median value is ~9 μM. The observation of identifiable peaks suggests that these materials can be utilized in non-invasive analysis for H_2O_2 sensing in biological specimens as well as environmental monitoring.

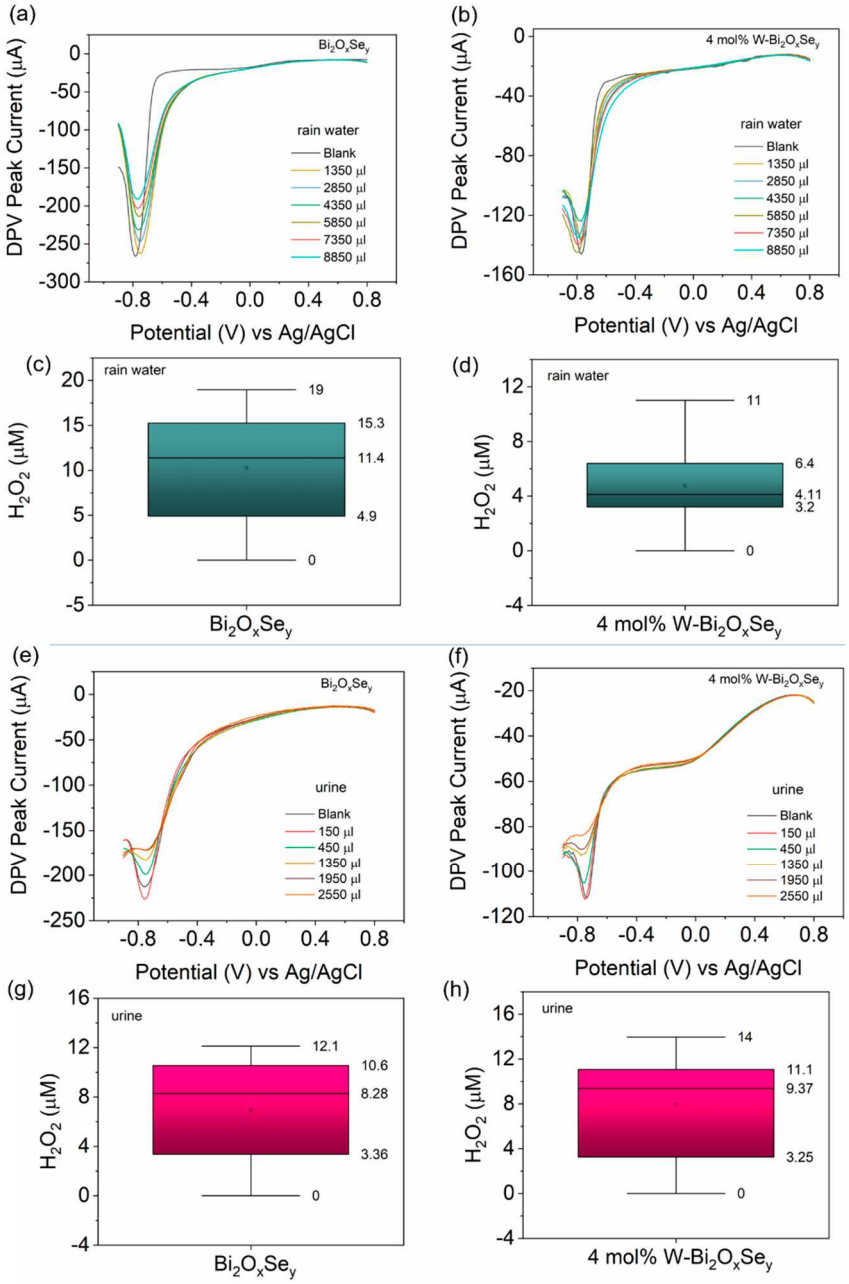

Figure 7. DPV scans for rainwater collected during a thunderstorm using (**a**) undoped and (**b**) 4 mol% W-doped $Bi_2O_xSe_y$ samples. (**c**,**d**) Corresponding box charts showing the estimated range of H_2O_2 in the rainwater samples. DPV scans for real urine using (**e**) undoped and (**f**) 4 mol% W-doped $Bi_2O_xSe_y$ samples. (**g**,**h**) Corresponding box charts showing the estimated range of H_2O_2 in the urine samples.

4. Conclusions

In summary, we synthesized W-doped $Bi_2O_xSe_y$ with varying doping amounts using a one-pot solution-phase method. The SEM analyses indicate the nanosheet to nanoparticle transformation with W-doping. XRD, EDX, and XPS analyses suggest that W may co-ordinate with Se and form an amorphous phase of bismuth oxyselenide and lead to a dominant bismuth oxide phase. This study provides valuable mechanistic insights into the electrochemical detection of H_2O_2 using $Bi_2O_xSe_y$ composites and highlights the complex role of W-doping on their electrochemical behavior. The synthesis of undoped and W-doped $Bi_2O_xSe_y$ nanostructures revealed a significant influence of W-doping on both material morphology and electrochemical sensitivity towards H_2O_2. While undoped $Bi_2O_xSe_y$ exhibited the highest sensitivity, 6 mol% W-doping led to complete insensitivity. These

contrasting results, observed through CV and DPV, highlight the complex interplay between composition and electrochemical performance. Moreover, the successful application of these materials in real-world samples, such as rainwater and urine, demonstrates their potential for practical sensing applications.

Supplementary Materials: The following supporting information can be downloaded at: https://www.mdpi.com/article/10.3390/electrochem5040030/s1, Figure S1: Wide XPS of 4 mol% W-doped $Bi_2O_xSe_y$ sample; Figure S2: (a) UV-Vis-NIR DRS for the samples. Tauc plots for (b) undoped, (c) 2 mol% W-doped, (d) 4 mol% W-doped, and (e) 6 mol% W-doped $Bi_2O_xSe_y$; Figure S3: (a) CV scans for the $Bi_2O_xSe_y$ with varying H_2O_2 concentrations (without stabilization). Linear fits for the (b) reduction peak and (c) oxidation peaks. # represents the change in the peak position from −0.66 V to −0.73 V (at 13.1 µM effective H_2O_2 concentration); Figure S4: DPV scans for accessing repeatability of the representative $Bi_2O_xSe_y$ electrode: (a) first run, (b) second run, (a) third run; Figure S5: (a) CV and (b) DPV of 4 mol% W-$Bi_2O_xSe_y$ with different analytes (a) CA response of 4 mol% W- $Bi_2O_xSe_y$. Table S1. Oxidation and reduction peaks observed in the CV scan in the blank electrolyte (after 50 cycles).

Author Contributions: Conceptualization, F.Y. and R.K.; methodology, P.D.W., R.K. and A.K.S.; software, R.K., F.Y. and A.K.S.; validation, R.K., F.Y. and A.K.S.; formal analysis, P.D.W., R.K., A.K.S. and F.Y.; investigation, P.D.W., R.K., A.K.S., O.K. and H.A.O.; resources, F.Y.; data curation, P.D.W., R.K., A.K.S., O.K. and H.A.O.; writing—original draft preparation, P.D.W. and R.K.; writing—review and editing, A.K.S. and F.Y.; visualization, P.D.W., R.K., A.K.S. and F.Y.; supervision, F.Y.; project administration, F.Y.; funding acquisition, F.Y. All authors have read and agreed to the published version of the manuscript.

Funding: F.Y. is thankful for the financial support from the U.S. National Science Foundation (NSF) under grant #DMR-2122044 and the U.S. Army Research Office (ARO) under grant # W911NF2210109.

Institutional Review Board Statement: The study was conducted in accordance with the Declaration of Helsinki, and approved by the Institutional Review Board (or Ethics Committee) of North Carolina Central University (IRB approval number is 1201786 and date of approval- 1 May 2024) for studies involving humans.

Informed Consent Statement: Informed consent was obtained from all subjects involved in the study.

Data Availability Statement: Data will be made available on request.

Acknowledgments: The authors are also thankful to Jeffrey Shallenberger and Jordan Meyet from MCL-Pennsylvania State University for helping with XPS and UV-Vis analyses. The authors acknowledge SMIF-Duke University for the powder XRD characterization.

Conflicts of Interest: The authors declare no conflicts of interest.

References

1. Bai, J.; Jiang, X. A Facile One-Pot Synthesis of Copper Sulfide-Decorated Reduced Graphene Oxide Composites for Enhanced Detecting of H_2O_2 in Biological Environments. *Anal. Chem.* **2013**, *85*, 8095–8101. [CrossRef] [PubMed]
2. Campanella, L.; Favero, G.; Giancola, D.; Tomassetti, M. Determination of Hydrogen Peroxide in Disinfectant Solutions Using a Biosensor with Two Antagonist Enzymes. *J. Pharm. Biomed. Anal.* **2003**, *32*, 737–751. [CrossRef] [PubMed]
3. Wang, X.; Martindale, J.L.; Liu, Y.; Holbrook, N.J. The Cellular Response to Oxidative Stress: Influences of Mitogen-Activated Protein Kinase Signalling Pathways on Cell Survival. *Biochem. J.* **1998**, *333*, 291–300. [CrossRef] [PubMed]
4. Lyublinskaya, O.; Antunes, F. Measuring Intracellular Concentration of Hydrogen Peroxide with the Use of Genetically Encoded H_2O_2 Biosensor HyPer. *Redox Biol.* **2019**, *24*, 101200. [CrossRef]
5. Teodoro, K.B.R.; Migliorini, F.L.; Christinelli, W.A.; Correa, D.S. Detection of Hydrogen Peroxide (H_2O_2) Using a Colorimetric Sensor Based on Cellulose Nanowhiskers and Silver Nanoparticles. *Carbohydr. Polym.* **2019**, *212*, 235–241. [CrossRef]
6. Zhang, Y.; Bai, X.; Wang, X.; Shiu, K.K.; Zhu, Y.; Jiang, H. Highly Sensitive Graphene-Pt Nanocomposites Amperometric Biosensor and Its Application in Living Cell H_2O_2 Detection. *Anal. Chem.* **2014**, *86*, 9459–9465. [CrossRef]
7. Gupta, R.; Singh, P.; Ganesan, V.; Koch, B.; Rastogi, P.K.; Yadav, D.K.; Sonkar, P.K. Palladium Nanoparticles Supported on Mesoporous Silica Microspheres for Enzyme-Free Amperometric Detection of H_2O_2 released from Living Cells. *Sens. Actuators B Chem.* **2018**, *276*, 517–525. [CrossRef]
8. Watt, B.E.; Proudfoot, A.T.; Vale, J.A. Hydrogen Peroxide Poisoning. *Toxicol. Rev.* **2004**, *23*, 51–57. [CrossRef]

9. Imlay, J.A.; Linn, S. Mutagenesis and Stress Responses Induced in Escherichia Coli by Hydrogen Peroxide. *J. Bacteriol.* **1987**, *169*, 2967–2976. [CrossRef]
10. Thatikayala, D.; Ponnamma, D.; Sadasivuni, K.; Cabibihan, J.-J.; Al-Ali, A.; Malik, R.; Min, B. Progress of Advanced Nanomaterials in the Non-Enzymatic Electrochemical Sensing of Glucose and H_2O_2. *Biosensors* **2020**, *10*, 151. [CrossRef]
11. Kulkarni, S.S.; Wu, C.T.; Sridhar, V.; Ponnusamy, V.K.; Chattopadhyay, S. Bi_2Te_3-Au Nanocomposite Schottky Junction with Peroxidase Activity for Glucose Sensing. *ACS Appl. Nano Mater.* **2022**, *5*, 15563–15573. [CrossRef]
12. McCurdy, W.H., Jr.; Bell, H.F. Titrimetric Determination of Hydrogen Peroxide in Alkaline Solution. *Talanta* **1966**, *13*, 925–928. [CrossRef] [PubMed]
13. Ito, E.; Watabe, S.; Morikawa, M.; Kodama, H.; Okada, R.; Miura, T. Detection of H_2O_2 by Fluorescence Correlation Spectroscopy. In *Methods in Enzymology*; Elsevier: Amsterdam, The Netherlands, 2013; Volume 526, pp. 135–143. ISBN 978-0-12-405883-5.
14. Şen, F.B.; Bener, M.; Bekdeşer, B.; Apak, R. Redox-Based Colorimetric Sensing of H_2O_2 after Removal of Antioxidants with ABTS Radical Oxidation. *Spectrochim. Acta Part A Mol. Biomol. Spectrosc.* **2021**, *248*, 119266. [CrossRef] [PubMed]
15. Takahashi, A.; Hashimoto, K.; Kumazawa, S.; Nakayama, T. Determination of Hydrogen Peroxide by High-Performance Liquid Chromatography with a Cation-Exchange Resin Gel Column and Electrochemical Detector. *Anal. Sci.* **1999**, *15*, 481–483. [CrossRef]
16. Chitara, B.; Limbu, T.B.; Orlando, J.D.; Vinodgopal, K.; Yan, F. 2-D Bi_2O_2Se Nanosheets for Nonenzymatic Electrochemical Detection of H_2O_2. *IEEE Sens. Lett.* **2020**, *4*, 1–4. [CrossRef]
17. Shringi, A.K.; Kumar, R.; Dennis, N.F.; Yan, F. Two-Dimensional Tellurium Nanosheets for the Efficient Nonenzymatic Electrochemical Detection of H_2O_2. *Chemosensors* **2024**, *12*, 17. [CrossRef]
18. Fan, H.; Zhang, S.; Ju, P.; Su, H.; Ai, S. Flower-like Bi_2Se_3 Nanostructures: Synthesis and Their Application for the Direct Electrochemistry of Hemoglobin and H_2O_2 Detection. *Electrochim. Acta* **2012**, *64*, 171–176. [CrossRef]
19. Othmani, A.; Derbali, M.; Kalfat, R.; Touati, F.; Dhaouadi, H. A Novel 1D/2D Bi_2S_3/g-C_3N_4 Core–Shell Nanocomposite as a Highly Performing H2O2 Non-Enzymatic Electrochemical Sensor. *J. Mater. Res. Technol.* **2021**, *15*, 5762–5775. [CrossRef]
20. Dhara, K.; Mahapatra, D.R. Recent Advances in Electrochemical Nonenzymatic Hydrogen Peroxide Sensors Based on Nanomaterials: A Review. *J. Mater. Sci.* **2019**, *54*, 12319–12357. [CrossRef]
21. Zou, X.; Wang, R.; Sun, Y.; Wang, C. Two-Dimensional Bi_2O_2Se Nanosheets for Sensitive and Fast-Response High-Temperature Photodetectors. *J. Mater.* **2023**, *9*, 1024–1031. [CrossRef]
22. Chen, Y.; Ma, W.; Tan, C.; Luo, M.; Zhou, W.; Yao, N.; Wang, H.; Zhang, L.; Xu, T.; Tong, T.; et al. Broadband Bi_2O_2Se Photodetectors from Infrared to Terahertz. *Adv. Funct. Mater.* **2021**, *31*, 2009554. [CrossRef]
23. Bae, J.K.; Cho, H.H.; Shin, H.; Kim, Y.; Ko, H.; Lee, S.J.; Megersa, D.D.; Gudena, G.T.; Chae, S.; Cho, I.S.; et al. One-Step Synthesis of Bi_2O_2Se Microstructures for Trace Oxygen Gas Sensor Application. *Sens. Actuators B Chem.* **2023**, *394*, 134398. [CrossRef]
24. Huang, C.; Yu, H. Two-Dimensional Bi_2O_2Se with High Mobility for High-Performance Polymer Solar Cells. *ACS Appl. Mater. Interfaces* **2020**, *12*, 19643–19654. [CrossRef] [PubMed]
25. Verma, D.; Liu, B.; Chen, T.C.; Li, L.J.; Lai, C.S. Bi_2O_2Se-Based Integrated Multifunctional Optoelectronics. *Nanoscale Adv.* **2022**, *4*, 3832–3844. [CrossRef] [PubMed]
26. Li, P.; Han, A.; Zhang, C.; He, X.; Zhang, J.; Zheng, D.; Cheng, L.; Li, L.J.; Miao, G.X.; Zhang, X.X. Mobility-Fluctuation-Controlled Linear Positive Magnetoresistance in 2D Semiconductor Bi_2O_2Se Nanoplates. *ACS Nano* **2020**, *14*, 11319–11326. [CrossRef] [PubMed]
27. Zhang, K.; Hu, C.; Kang, X.; Wang, S.; Xi, Y.; Liu, H. Synthesis and Thermoelectric Properties of Bi_2O_2Se Nanosheets. *Mater. Res. Bull.* **2013**, *48*, 3968–3972. [CrossRef]
28. Wang, Z.; Liu, L.; Zhai, K.; Nie, A.; Xiang, J.; Mu, C.; Wen, F.; Wang, B.; Shu, Y.; Xue, T.; et al. An Ultrasensitive Plasmonic Sensor Based on 2D Ferroelectric Bi_2O_2Se. *Small* **2023**, *19*, 2303026. [CrossRef]
29. Kang, M.; Chai, H.J.; Jeong, H.B.; Park, C.; Jung, I.Y.; Park, E.; Çiçek, M.M.; Lee, I.; Bae, B.S.; Durgun, E.; et al. Low-Temperature and High-Quality Growth of Bi_2O_2Se Layered Semiconductors via Cracking Metal-Organic Chemical Vapor Deposition. *ACS Nano* **2021**, *15*, 8715–8723. [CrossRef]
30. Tao, H.; Wang, T.; Li, D.; Xing, J.; Li, G. Preparation, Properties, and Applications of Bi_2O_2Se Thin Films: A Review. *J. Semicond.* **2023**, *44*, 031001. [CrossRef]
31. Luo, P.; Zhuge, F.; Wang, F.; Lian, L.; Liu, K.; Zhang, J.; Zhai, T. PbSe Quantum Dots Sensitized High-Mobility Bi_2O_2Se Nanosheets for High-Performance and Broadband Photodetection beyond 2 Mm. *ACS Nano* **2019**, *13*, 9028–9037. [CrossRef]
32. Wu, J.; Yuan, H.; Meng, M.; Chen, C.; Sun, Y.; Chen, Z.; Dang, W.; Tan, C.; Liu, Y.; Yin, J.; et al. High Electron Mobility and Quantum Oscillations in Non-Encapsulated Ultrathin Semiconducting Bi_2O_2Se. *Nat. Nanotechnol.* **2017**, *12*, 530–534. [CrossRef] [PubMed]
33. Ghosh, T.; Samanta, M.; Vasdev, A.; Dolui, K.; Ghatak, J.; Das, T.; Sheet, G.; Biswas, K. Ultrathin Free-Standing Nanosheets of Bi_2O_2Se: Room Temperature Ferroelectricity in Self-Assembled Charged Layered Heterostructure. *Nano Lett.* **2019**, *19*, 5703–5709. [CrossRef] [PubMed]
34. Walimbe, P.D.; Kumar, R.; Shringi, A.K.; Keelson, O.; Ouma, H.A.; Yan, F. Electrochemical Detection of H_2O_2 Using Bi_2O_3/Bi_2O_2Se Nanocomposites. *Nanomaterials* **2024**, *14*, 1592. [CrossRef] [PubMed]

35. Ray, C.; Dutta, S.; Roy, A.; Sahoo, R.; Pal, T. Redox Mediated Synthesis of Hierarchical Bi_2O_3/MnO_2 Nanoflowers: A Non-Enzymatic Hydrogen Peroxide Electrochemical Sensor. *Dalton Trans.* **2016**, *45*, 4780–4790. [CrossRef]
36. Periasamy, A.P.; Yang, S.; Chen, S.-M. Preparation and Characterization of Bismuth Oxide Nanoparticles-Multiwalled Carbon Nanotube Composite for the Development of Horseradish Peroxidase Based H_2O_2 Biosensor. *Talanta* **2011**, *87*, 15–23. [CrossRef]